Valley caloritronics in a photodriven heterojunction of Dirac materials

Priyadarshini Kapri [⬤],[*] Bashab Dey, and Tarun Kanti Ghosh

Department of Physics, Indian Institute of Technology Kanpur, Kanpur 208 016, India

We consider a lateral heterojunction where the left and right leads are made of monolayer graphene and the middle region is made of a gapped tilted Dirac material (borophene or quinoid graphene) illuminated with off-resonant circularly polarized radiation. The tilt parameter v_t makes the band gap indirect and smaller in magnitude as compared to Dirac materials without tilt. Exposure to radiation makes the band gaps of the central region valley dependent, which show their signatures as valley-polarized charge and thermal currents, thereby causing a valley Seebeck effect. We study the variation of the valley-polarized electrical conductance, thermal conductance, thermopower, and figure of merit of this junction with chemical potential μ and a tunable gap parameter η. For nonzero η, all the valley-polarized quantities are peaked at certain values of chemical potential and then vanish asymptotically. An increase in the gap parameter enhances the valley thermopower and valley figure of merit, whereas the valley conductances (electrical and thermal) show nonmonotonic behavior with η. We also compare the valley-polarized quantities with their corresponding charge counterparts (effective contribution from both valleys). The charge thermopower and the charge figure of merit behave nonmonotonically with η and the charge conductances (electrical and thermal) depict a decreasing trend with η. Furthermore, the tilt parameter reduces the effective transmission of carriers through the junction, thereby diminishing all the charge- and valley-polarized quantities. As the gaps in the dispersion can be adjusted by varying the intensity of light as well as the Semenoff mass, the tunability of this junction with regard to its thermoelectric properties may be experimentally realizable.

I. INTRODUCTION

Thermoelectric materials have attracted immense interest in energy efficient device applications [1–13]. The efficiency of power generation in such devices depends on the interplay between their electronic and thermal performances and it is characterized by a dimensionless quantity called the figure of merit, $ZT = S^2 \sigma T/\kappa$, where σ, κ, and S denote electrical conductivity, thermal conductivity, and the Seebeck coefficient (thermopower), respectively, with T being the absolute temperature. In bulk materials, the factors in the expression of ZT are mutually coupled in such a way that it is difficult to control them independently, and hence improve ZT. The techniques used to improve the figure of merit rely on enhancing the power factor (σS^2) and lowering the thermal conductivity. One of the important proposals is the nanostructuring of materials which enhances thermoelectric efficiency due to the sharply peaked density of states (DOS) of the carriers in low-dimensional materials [1,14]. Another useful method is engineering the band structure [15,16] in conjunction with nanostructuring to lower the thermal conductivity. Further, the use of semimetals with a large electron-hole asymmetry can enhance the thermoelectric coefficients [17].

Advancements in fabrication technologies have opened up new ways of exploring two-dimensional (2D) materials for thermoelectric applications [7–11]. Since the realization of graphene [18,19] there have been numerous experimen-

tal and theoretical studies of quasi-2D materials supporting Dirac cones such as silicene [20], germanene [21], and MoS$_2$ [22]. Recently, there has been immense interest in the synthesis of 2D crystalline boron structures, generally known as borophene [23–25]. One of them is 8-*Pmmn* borophene, which is a zero gap semiconductor with tilted anisotropic Dirac cones [26–28] and can be thought of as topologically equivalent to quinoid graphene [29,30]. The bulk optical [31], magnetotransport [32], collective modes [33], Floquet states [34], and thermoelectric properties [35] of this borophene structure have been studied extensively. Another experimentally synthesized allotrope of boron is β_{12} borophene whose band structure and electronic properties have been extensively studied [36,37]. In addition, very recent success in integrating dissimilar two-dimensional (2D) materials [38], which is essential for nanoelectronic applications, has opened a new direction for studying the thermoelectricity in junction devices of different materials. In Ref. [38], the authors have reported the covalent lateral stitching of borophene-graphene, resulting in the rare realization of a 2D lateral heterostructure where the lateral interfaces are atomically sharp despite an imperfect crystallographic lattice and symmetry matching. Furthermore, a graphene/quinoid graphene/graphene junction can be realized by taking a single graphene sheet, where the middle region is deformed (quinoid graphene) by applying a uniaxial strain.

Recently, the concept of valleytronics [39–42], similar to spintronics [43–48], has become popular. In valleytronic devices, the information is carried by the valley degree of freedom of the charge carriers. The generation of valley

_____

*pkapri@iitk.ac.in

polarization and optically excited valley-polarized current in various materials has been studied theoretically as well as experimentally [49–52]. The harnessing of internal degrees of freedom such as the spin/valley of the charge carriers by applying a thermal gradient and the associated phenomena are called spin/valley caloritronics.

Motivated by the above discussion, we study the thermoelectric effects of a nanojunction system where the left and right electrodes are made of graphene and the middle region is made of a 2D Dirac material having tilted anisotropic Dirac cones, such as borophene or quinoid graphene. The middle region has different on-site energies on the two sublattices and is subjected to circularly polarized electromagnetic radiation. It results in valley-dependent bands at the two Dirac points and hence a valley-dependent transmission probability. Thus, in analogy with the spin caloritronics studies, a thermally activated quantum transport of the valley degree of freedom of the charge carriers can be achieved. Our goal is to study thermally driven valley-polarized properties, known as valley caloritronics, and compare them with that of the charge caloritronics in detail.

This paper is organized as follows. In Sec. II, we present the basic information of the lateral junction (Sec. II A) and the definitions of different thermoelectric coefficients (Sec. II B). All the numerical results and their corresponding discussions are presented in Sec. III. Finally, we conclude and summarize our main results in Sec. IV.

II. MODEL AND THEORETICAL METHODS

Here, we first present the essential information on the junction characterized by quasiballistic transport. Later, we will present a general description of the Seebeck coefficient, electrical conductance, thermal conductance, and figure of merit for any junction device. The discussions in Sec. II B are applicable to any junction characterized by quasiballistic transport.

A. Basic information on the junction

We consider a two-dimensional junction system placed on the xy plane at room temperature as shown in Fig. 1. The left ($x < 0$) and right ($x > L$) leads are made of graphene sheets, while the middle region ($0 < x < L$) is made of a 2D material hosting tilted anisotropic Dirac dispersion (it can be considered as borophene or quinoid graphene) with a mass gap at low energy. Further, it is assumed that the middle region is subjected to circularly polarized electromagnetic radiation where the photon energy satisfies the off-resonant condition, i.e., the photon energy is much higher than the bandwidth of the undriven lattice in the middle region of the system. The off-resonant circularly polarized light induces a gap in the energy dispersion.

The Hamiltonian for the charge carriers in a graphene sheet in the vicinity of the Dirac points is given by [29]

$$H_G = \zeta \hbar v_F (\sigma_x k_x + \zeta \sigma_y k_y), \qquad (1)$$

where $\zeta = \pm$ denotes two independent Dirac points, $v_F = 10^6$ m/s is the Fermi velocity, and σ_x, σ_y are the Pauli matrices denoting the sublattice degrees of freedom. The
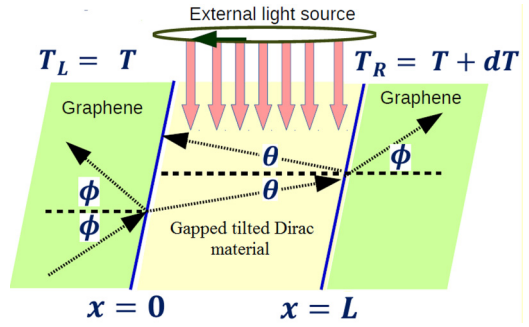

FIG. 1. Schematic illustration of the reflection and the transmission processes across a two-dimensional lateral junction of Dirac material. The middle region of the junction is illuminated by circularly polarized electromagnetic radiation for the opening of valley-dependent gaps. The angles ϕ and θ denote the incident angles at the first and second interfaces, respectively.

corresponding energy dispersion of the Hamiltonian in Eq. (1) is given by $E_\lambda(k) = \lambda \hbar v_F k$, independent of the valley pseudospin ζ, where $\lambda = \pm$ denotes the conduction and valence bands, respectively. The corresponding eigenfunctions are given by

$$\Psi_G^{\lambda,\zeta}(\mathbf{r}) = \frac{e^{i\mathbf{k}\cdot\mathbf{r}}}{\sqrt{2}} \begin{pmatrix} 1 \\ \zeta \lambda e^{i\zeta\phi} \end{pmatrix}, \qquad (2)$$
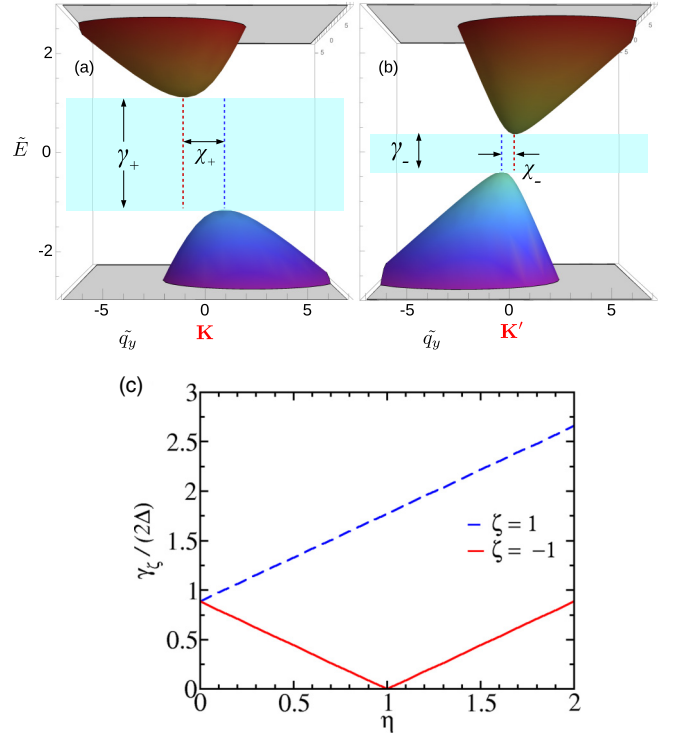
where $\phi = \tan^{-1} k_y/k_x$.

FIG. 2. (a), (b) Band structure of borophene around the two Dirac points for $\eta = 0.5$. Here, γ_ζ is the magnitude of the indirect band gap and χ_ζ is the corresponding shift. The dimensionless variables $\tilde{E}$ and $\tilde{q}_y$ are defined as $\tilde{E} = E/\Delta$ and $\tilde{q}_y = \hbar v_F q_y/\Delta$, where Δ is the photoinduced mass. (c) The indirect band gaps γ_ζ in units of 2Δ as a function of η.

The effective Floquet Hamiltonian, describing the charge carriers of the middle region (tilted anisotropic borophene or quinoid graphene) subjected to circularly polarized electromagnetic radiation, in the vicinity of the two independent Dirac points can be written as [53] (see Appendix A)

$$H_B = \zeta\hbar[v_x q_x \sigma_x + \zeta v_y q_y \sigma_y + v_t \sigma_0 q_y] + \Delta_\zeta \sigma_z. \quad (3)$$

Here, σ_0 is the 2×2 identity matrix and $\Delta_\zeta = M + \zeta\Delta$ is the net valley-dependent mass resulting from the valley-dependent photoinduced mass $\zeta\Delta$ [54] and different on-site energies on the two sublattices $\pm M$ [55], with M being the Semenoff mass. The photoinduced mass $\Delta = (eA_0)^2 v_x v_y/(\hbar\omega)$ is proportional to the intensity of light, which can be tuned experimentally. A tunable Semenoff mass has been experimentally achieved in graphene by placing it appropriately on a hexagonal boron nitride substrate [56] or by applying an electric field normal to its plane [57] (which breaks inversion symmetry). Using similar techniques, the creation of such a mass gap may be possible in borophene as well, although its experimental realization is still not known. We define a dimensionless parameter $\eta = M/\Delta$ such that $\Delta_\zeta = \Delta(\eta + \zeta)$. Here, (v_x, v_y, v_t) are the direction-dependent velocities where v_t (tilt parameter) is responsible for the tilt in energy dispersion. The values of these velocities for borophene are $v_x = 0.86v_F$, $v_y = 0.69v_F$, and $v_t = 0.32v_F$ [27]. The energy dispersion and the corresponding wave functions associated with the Hamiltonian in Eq. (3) are given by

$$E_{\lambda,\zeta}(\mathbf{q}) = \zeta\hbar q v_t \sin\theta + \lambda\sqrt{\Delta_\zeta^2 + [\hbar q \Lambda(\theta)]^2}, \quad (4)$$

and

$$\Psi_B^{\lambda,\zeta}(\mathbf{r}) = \frac{e^{i\mathbf{q}\cdot\mathbf{r}}}{\sqrt{2}}\begin{pmatrix} 1 \\ \frac{\zeta\hbar q \Lambda(\theta)e^{i\zeta\delta}}{\Delta_\zeta + \lambda\sqrt{\Delta_\zeta^2 + [\hbar q \Lambda(\theta)]^2}} \end{pmatrix}, \quad (5)$$

where $\delta = \tan^{-1}(v_y q_y/v_x q_x) = \tan^{-1}(\delta_a \tan\theta)$ with $\delta_a = v_y/v_x$, $\theta = \tan^{-1}(q_y/q_x)$, and $\Lambda(\theta) = \sqrt{v_x^2 \cos^2\theta + v_y^2 \sin^2\theta}$ having a dimension of velocity.

The band structure of borophene in the two valleys with valley-dependent masses is shown in Fig. 2 for $\eta = 0.5$. The system is an insulator with valley-dependent indirect band gaps γ_ζ. The shift χ_ζ between maxima of the valence band and minima of the conduction band in both valleys is along the q_y axis. The magnitude of the indirect gaps and the shifts are given as

$$\gamma_\zeta = 2\Delta_\zeta\sqrt{1 - \frac{v_t^2}{v_y^2}}, \quad \chi_\zeta = \frac{2v_t\Delta_\zeta}{\hbar v_y \sqrt{v_y^2 - v_t^2}}. \quad (6)$$

Equation (6) reveals that the band gaps reduce due to tilt and decrease monotonically with v_t for $v_t < v_y$ while the shifts corresponding to the gaps increase. For $\eta > 0$, the band gap at the K' valley is smaller than at the K valley. So, the effective band gap of the system is γ_-. The direct gaps at the original Dirac points are equal to $2\Delta_\zeta$. The magnitude of the gap at the K valley monotonically increases with η, whereas for the K' valley it initially decreases with η (for $\eta < 1$), vanishes at $\eta = 1$, and then starts to increase again for $\eta > 1$ [see Fig. 2(c)].

The middle region can be reduced to a gapped graphene by setting $v_t = 0$ and $v_x = v_y = v_F$, so that the junction becomes a graphene/gapped-graphene/graphene junction. If the Fermi energy lies in the gap, the middle region behaves as a topological insulator when $M < \Delta$, otherwise it is a trivial insulator. In the topological insulating state, the edge states contribute to the transport quantities. Since our system is kept at room temperature, the contribution from the bulk states would dominate over the edge states' contribution [58].

Suppose an electron from the left lead is injected with an energy ϵ and incident angle ϕ. The valley-dependent transmission probability $\mathcal{T}_\zeta(\epsilon, \phi) = |t_\zeta(\epsilon, \phi)|^2$ of the electron from the left to right lead is obtained as (see Appendix B)

$$\mathcal{T}_\zeta(\epsilon, \phi) = \frac{4p_\zeta^2 \cos^2\phi(1 + \cos 2\delta)}{\left(2\sqrt{2}p_\zeta \cos\phi \cos\delta\right)^2 + \left[1 + p_\zeta^2 - 2p_\zeta \cos(\phi - \delta)\right]\left[1 + p_\zeta^2 + 2p_\zeta \cos(\phi + \delta)\right][1 - \cos(2qL\cos\theta)]}, \quad (7)$$

where p_ζ is given by

$$p_\zeta = \frac{\hbar q \Lambda(\theta)}{\Delta_\zeta + \sqrt{\Delta_\zeta^2 + [\hbar q \Lambda(\theta)]^2}}. \quad (8)$$

The values of q and θ in the expression of p_ζ can be obtained by solving the following two coupled equations,

$$q \sin\theta = k \sin\phi,$$

$$q = \frac{\zeta\epsilon v_t \sin\theta \mp \sqrt{\Lambda^2(\theta)(\epsilon^2 - \Delta_\zeta^2) + (v_t\Delta_\zeta \sin\theta)^2}}{\hbar[(v_t \sin\theta)^2 - \Lambda^2(\theta)]}. \quad (9)$$

We define the effective transmission coefficient for current along the x direction at a given energy ϵ as $\mathcal{T}_\zeta(\epsilon) = \int_{-\pi/2}^{\pi/2} \mathcal{T}_\zeta(\epsilon, \phi) \cos\phi\, d\phi$. In Figs. 3 and 4, $\mathcal{T}_\zeta(\epsilon)$ vs ϵ is plotted for two conditions: (i) $v_t = 0$, $v_x = v_y = v_F$ and (ii) $v_t \neq 0$,

$v_x = v_y = v_F$. The oscillations in $\mathcal{T}_\zeta(\epsilon)$ in Fig. 4 appear due to the $\cos(2qL\cos\theta)$ term [see Eq. (7)], where q is a function of ϵ. In the case of $v_x = v_y = v_F$, $v_t = 0$, and $E \gg \Delta_\zeta$, the values of the ϕ and δ become equal and p_ζ becomes ~ 1, which eventually yields the coefficient of $[1 - \cos(2qL\cos\theta)]$ to be ~ 0 and thus $\mathcal{T}_\zeta(\epsilon, \phi)$ becomes ~ 1 [see Eq. (7)] and $\mathcal{T}_\zeta(\epsilon) \sim 2$. As a result, no such noticeable oscillations are obtained [see the red curves of Figs. 3(a) and 3(b)]. The physics behind this can be explained using the concept of electron wave interference—when $v_t = 0$, $v_x = v_y = v_F$, and $E \gg \Delta_\zeta$, the system can be viewed as a single graphene sheet without any barrier. Thus, almost all the incoming electron waves from the left lead get transmitted to the right lead, leaving almost no reflected wave and thereby causing no interference. If the band gap is further increased, the probability of the reflection of electron waves from the interface increases; so the reflected
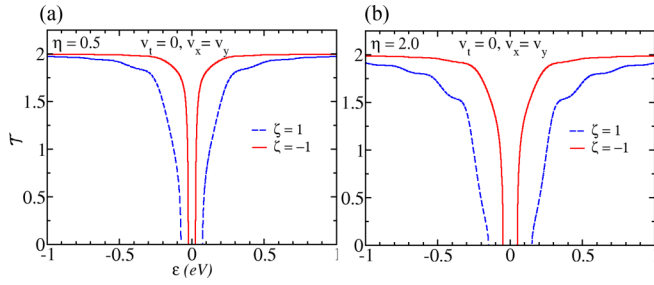
FIG. 3. $\mathcal{T}_\zeta(\epsilon)$ vs ϵ for (a) $\eta = 0.5$, (b) $\eta = 2$ when $v_t = 0$, $v_x = v_y = v_F$.

and the transmitted electron waves begin to interfere. This results in oscillations in the transmission probability for the $v_t = 0$, $v_x = v_y = v_F$ case as well [see the blue curves in Figs. 3(a) and 3(b)]. Furthermore, the K valley has smaller $\mathcal{T}_\zeta(\epsilon)$ as compared to the K' valley. It can be understood using the analogy of transmission through a rectangular potential barrier. If the middle region is considered as a potential barrier with a barrier height Δ_ζ, the transmission probability is smaller for a larger barrier height for the considered range of incident energies above the barrier. Since $\Delta_+ > \Delta_-$, the K valley allows lesser transmission than K'.

The tilted velocity term diminishes $\mathcal{T}_\zeta(\epsilon)$, and as for $v_t \neq 0$ the transmission probability as a function of incident angle shows more of a deviation from 1 compared to the $v_t = 0$ case (see Figs. 9–11). Moreover, the $\mathcal{T}_\zeta(\epsilon)$ is almost electron-hole symmetric (see Figs. 3 and 4), although v_t breaks the electron-hole symmetry in the band structure (see Fig. 2).

B. Thermoelectric coefficients

A detailed derivation of the thermoelectric coefficients is given in Appendix C. The valley-resolved Seebeck coefficient S_ζ for a small temperature difference dT is given as

$$S_\zeta = -\frac{dV_\zeta}{dT}\bigg|_{dI_\zeta = 0} = -\frac{L_\zeta^{(1)}}{eTL_\zeta^{(0)}}, \tag{10}$$

where dV_ζ are the valley-resolved thermoemfs induced between the cold and hot leads and $L_\zeta^{(\alpha)}$ are the kinetic coefficients for quasiballistic transport given by

$$L_\zeta^{(\alpha)} = \int_{-\pi/2}^{\pi/2} d\phi \cos\phi \int_{-\infty}^{\infty} \mathcal{T}_\zeta(\epsilon, \phi) N(\epsilon)(\epsilon - \mu)^\alpha$$
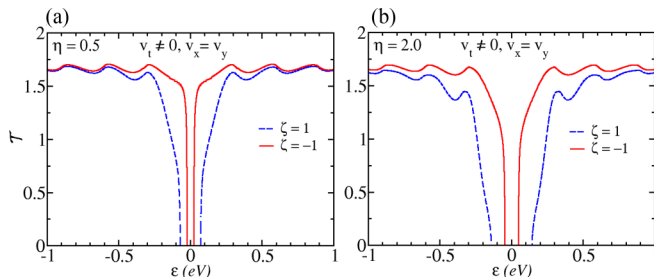$$\times \left(-\frac{\partial f}{\partial \epsilon}\right) d\epsilon, \tag{11}$$

FIG. 4. $\mathcal{T}_\zeta(\epsilon)$ vs ϵ for (a) $\eta = 0.5$, (b) $\eta = 2$ when $v_t \neq 0$, $v_x = v_y = v_F$.

with $\alpha = 0, 1, 2$.

At zero external bias voltage ($V_B = 0$), the valley-resolved electrical conductance G_ζ can be expressed as

$$G_\zeta = \frac{dI_\zeta}{dV}\bigg|_{V_B = 0} = \frac{2e^2}{h} L_\zeta^{(0)}, \tag{12}$$

where I_ζ is the valley-dependent charge current given in Eq. (C1).

The valley-resolved thermal conductance k_ζ^{el} associated with the valley-dependent thermal currents J_ζ^{el} can be expressed in terms of the kinetic coefficients $L_\zeta^{(\alpha)}$ [see Eq. (11)] as [59,60]

$$k_\zeta^{\text{el}} = \frac{2}{h}\frac{L_\zeta^{(2)}}{T} + \frac{2e}{h}L_\zeta^{(1)}S_\zeta. \tag{13}$$

The total charge and thermal conductance are defined as $G_c = G_+ + G_-$ and $k_c^{\text{el}} = k_+^{\text{el}} + k_-^{\text{el}}$. Similar to Refs. [46,47], we define the charge Seebeck coefficient as $S_c = (S_+ G_+ + S_- G_-)/(G_+ + G_-)$. The charge Seebeck coefficient can be viewed as the effective thermoemf generated between the two leads per unit temperature difference.

In this system, the carriers in the two valleys have unequal transmission probabilities owing to the distinctive nature of the valley gaps. So, the heat and particle flux in the two valleys differ, giving rise to valley-polarized charge currents ($I_v = |I_+ - I_-|$) and thermal currents ($J_v^{\text{el}} = |J_+^{\text{el}} - J_-^{\text{el}}|$). This leads to different induced voltages in the two valleys at the cold lead. Thus, the two valleys act as two conducting channels having different thermopowers present within the same system. Since the transfer of electrons between the valleys is prohibited due to the large separation of the valleys in (quasi)momentum space and the absence of any valley-mixing mechanism, a valley emf ($dV_+ - dV_-$) exists. This phenomenon can be termed as the valley Seebeck effect analogous to the spin Seebeck effect [43]. It refers to the generation of a valley voltage resulting from a temperature gradient.

Using the same analogy as in Ref. [48] for the spin Seebeck coefficient, the valley Seebeck coefficient is defined as $S_v = |S_+ - S_-|$. Similar to the spin Seebeck effect [43], the valley Seebeck coefficient can be viewed as the potential difference between charge carriers of the two valleys in the cold lead per unit temperature difference. Similar to the valley current, the valley-polarized electrical conductance and the valley-polarized thermal conductance can be defined as $G_v = |G_+ - G_-|$ and $k_v^{\text{el}} = |k_+^{\text{el}} - k_-^{\text{el}}|$, respectively.

One of the challenges in fabricating thermoelectric devices is to obtain optimal conditions which ensure the operation of the device with maximum power output at the best possible efficiency. The efficiency of the system depends upon a quantity called the figure of merit $Z_c T$, which is defined as

$$Z_c T = \frac{S_c^2 G_c}{k_c^{\text{el}} + k^{\text{ph}}} T, \tag{14}$$

where S_c is the charge Seebeck coefficient, G_c is the charge conductance, k_c^{el} is the thermal conductance of the carriers, k_{ph} is the phonon's thermal conductance owing to the involvement of the lattice structure, and T is the absolute temperature. The possibility of extracting the valley thermoemf for power
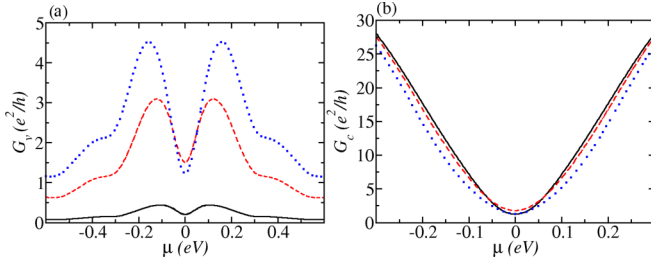
FIG. 5. Variation of (a) valley conductance G_v and (b) charge conductance G_c as a function of chemical potential μ for different values of η: $\eta = 0.1$ (black solid), $\eta = 0.8$ (red dashed), and $\eta = 1.5$ (blue dotted).

generation allows us to define the valley figure of merit $Z_v T = \frac{S_v^2 G_v}{k_c^{el}}$ of this device using the same analogy as the spin figure of merit in Refs. [48,61–63].

In the context of a phononic contribution to thermal conductance, we would like to mention that the Debye temperature in borophene has a high value of about 2000 K [64,65] due to the strong bonding. Further, graphene has also a higher Debye temperature $\theta_D = 2300$ K, approximately an order of magnitude higher than for typical metals. Thus, the room temperature (300 K) is safely assumed to be low with respect to the high Debye temperatures of borophene and graphene. Due to this reason, the phonon population is expected to be low at room temperature, which diminishes the possibility of phonon-phonon inelastic scattering events. Henceforth we neglect the phonon's contribution in thermal conductance.

III. RESULTS AND DISCUSSION

Here, we present numerical results of different thermoelectric properties of the junction subjected to the off-resonant Floquet radiation. For our numerical analysis, we choose the parameters $v_x = v_y = v_F$, $v_t = 0.32 v_F$, and $\Delta = 0.05$ eV. The dimensionless parameter $\eta = M/\Delta$ is varied in the range $[0 : 1.5]$. It should be noted that by further increasing the η value, the conductance in the K valley vanishes in the low chemical potential region. As our main goal is to study the valley-polarized properties, to get nonzero values of the conductance for both the valleys, we choose the maximum $\eta = 1.5$. The temperature of the cold lead is maintained at $T = 300$ K and that of the hot lead is $T + dT$ where $dT \ll T$. The dimensions of system are taken as $(L, W) = (50, 30)$ nm.

A. Valley electrical conductance

The variation of G_v and G_c with chemical potential μ for different values of η are shown in Figs. 5(a) and 5(b), respectively.

1. Dependence on chemical potential

The valley-polarized conductance G_v has peaks at $\pm \mu_p(\eta)$ and a local minimum at $\mu = 0$ [Fig. 5(a)]. This feature is also present when the middle region is gapped graphene with unequal masses Δ_ζ in the two valleys, which indicates that tilt is not responsible for the peaks. The appearance of peaks can be explained using an analogy with transmission through

a rectangular barrier. For gapped graphene, the dispersion can be approximated as $E_\zeta \approx \Delta_\zeta + \frac{\hbar^2 q^2}{2(\Delta_\zeta/v_F^2)}$ near the band minima/maxima. So, the middle region can be viewed as a potential barrier with valley-dependent barrier heights ($V_\zeta = \Delta_\zeta$) and effective masses ($m_\zeta = \Delta_\zeta/v_F^2$). The rate of increase of transmission $\mathcal{T}(\epsilon)$ with $|\epsilon|$ for smaller mass (Δ_-) is higher than that with larger mass (Δ_-) for energies just above the barrier (see Figs. 3 and 4). Since $G_\zeta(\epsilon)$ is proportional to $\mathcal{T}_\zeta(\epsilon)$, G_+ increases slowly with μ, resembling a quadratic growth, while G_- rises sharply, resembling almost a linear growth due to the smaller mass. For a higher value of $|\mu|$, the effect of mass in the dispersion becomes negligible in both valleys, which results in an almost similar variation of their conductances with $|\mu|$. Due to this nature, G_v increases with $|\mu|$ initially, attains a maximum (peak), and then decreases asymptotically to zero at higher $|\mu|$.

On the other hand, G_c increases monotonically with an increase in $|\mu|$ [Fig. 5(b)]. This is primarily due to the increase in the number of available conducting channels $N(\epsilon)$ in the leads with an increase in $|\epsilon|$. As expected, G_c is always greater than G_v for a given η.

2. Dependence on gap parameter

The valley conductance G_v increases with the increasing strength of η for $\eta < 1$ and starts to decrease with η for $\eta > 1$. This can be explained as follows: Since a larger gap corresponds to lesser $\mathcal{T}_\zeta(\epsilon)$, the increase in η lowers G_+, owing to the monotonic rise in Δ_+ with η [see Fig. 2(c)]. Similarly, due to the nonmonotonic variation of Δ_-, G_- initially increases with η, attains a maximum value at $\eta = 1$, and then starts to decrease with η. Since G_- increases while G_+ decreases with η for $\eta < 1$, their difference gets enhanced with η. For $\eta > 1$, both G_+ and G_- decrease with η, but the rate of decrease of G_- is more than that of G_+. As a result, G_v gets diminished with η for $\eta > 1$. For $\eta \to 0$, we get $\Delta_\zeta \to \zeta \Delta$, which yields $\mathcal{T}_+(\epsilon, \phi) = \mathcal{T}_-(\epsilon, -\phi)$. On integrating out ϕ, both the valleys give the same value of transmission at a given energy. Hence, $G_v \to 0$ as $\eta \to 0$.

Figure 5(b) reveals that G_c gets diminished (though the change is small, but noticeable) with increasing η, away from the low chemical potential regime. Near the low chemical potential region, there are crossovers in the conductance plots.

The tilt v_t diminishes G_ζ in each valley, which results in a lowering of G_c. It is found that G_v also decreases with v_t, since v_t diminishes $[\mathcal{T}_-(\epsilon) - \mathcal{T}_+(\epsilon)]$ as well (see Figs. 3 and 4). It is interesting to note that charge and valley conductances show a high degree of electron-hole symmetry despite the fact that the spectrum in the middle region is electron-hole asymmetric due to nonzero v_t. Similar behavior is shown in bulk borophene [35].

B. Valley Seebeck coefficient (thermopower)

The valley and charge Seebeck coefficients S_v and S_c (in units of k_B/e) as a function of the chemical potential μ for various values of η are shown in Figs. 6(a) and 6(b), respectively.
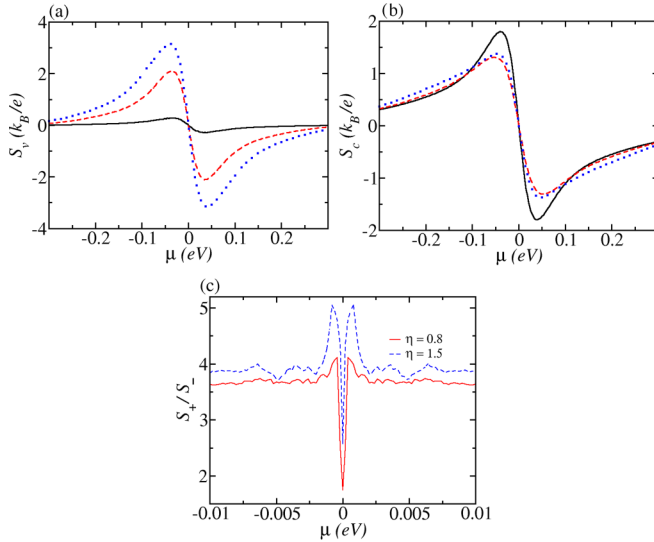
FIG. 6. Variation of (a) valley Seebeck coefficient S_v, (b) charge Seebeck coefficient S_c, and (c) ratio of S_+ and S_- as a function of chemical potential μ for different values of η: $\eta = 0.1$ (black solid), $\eta = 0.8$ (red dashed), and $\eta = 1.5$ (blue dotted).

1. Dependence on chemical potential

Both S_v and S_c display a local maxima (minima) at $\mu_s \sim 0.04$ (-0.04) eV on variation with μ. The value of μ_s is roughly independent of η. The maxima/minima in the thermopower arises due to the term $(\epsilon - \mu)(-\frac{\partial f}{\partial \epsilon})$ in the numerator of the Seebeck coefficient [see Eq. (10)]. There is a change in sign of S while there is a change in sign of μ [due to the $(\epsilon - \mu)$ term in the numerator of S]. It indicates the change in the electrical nature of the charge carriers as μ changes sign. When μ lies in the conduction (valence) band, thermally activated electrons (holes) propagate opposite (parallel) to the temperature gradient, which results in negative (positive) thermopower. Similar to the conductance, the electron-hole symmetry is nearly perfect in the absolute value of Seebeck coefficients.

2. Dependence on gap parameter

The absolute values of S_v increase with η at a given chemical potential. This can be explained as follows: From the definition of the Seebeck coefficient $S_\zeta \sim \frac{L_\zeta^{(1)}}{G_\zeta}$, we can say that an increase in $L_\zeta^{(1)}$ and a decrease in G_ζ with η aids in enhancing the value of S_ζ. Since $L_+^{(1)}$ increases and G_+ decreases with η, S_+ starts to gain weight as we increase η. Similarly, S_- initially decreases with η, attains minimum at $\eta = 1$, and again starts to increase. Though S_+ and S_- show a different nature of variation with η, their difference as a function of η is mainly dictated by S_+. This happens because the K valley's contribution in thermopower changes more rapidly with η as compared to the K' valley. The behavior of the valley thermopower as a function of η can be understood from Fig. 6(c) also. As the ratio of S_+ and S_- increases with η, the valley thermopower gets enhanced with an increasing strength of η. The reason behind this can be understood from Fig. 4, as it reveals that with increasing η from 0.5 to 2.0, the

rate of change in $\mathcal{T}(\epsilon)$ in the K valley is more than that in the K' valley.

For the chemical potential $|\mu| < 0.08$ eV, the charge thermopower S_c decreases with η for $\eta < 1$, attains minima around $\eta = 1$, and then starts increasing again. For $|\mu| > 0.08$ eV, an increase in η aids in enhancing S_c, though the enhancement is quite small. So S_v and S_c behave differently with η which is mainly due to the different weights of the K and K' channels' contribution in their definitions. It seems that on increasing the strength of η even more, one can achieve a higher valley thermopower. But it is not possible, as for such a higher value of η, there will be no available channel to conduct in the low chemical potential regime.

It is worth mentioning that S_v decreases with v_t. Though v_t diminishes G_ζ (denominator of S_ζ), it lowers $L_\zeta^{(1)}$ (numerator of S_ζ), too. Hence, the contribution of $(\frac{L_+^{(1)}}{G_+} - \frac{L_-^{(1)}}{G_-})$ (see the definition of S_v) decreases as we increase v_t. The charge thermopower also behaves similarly as a function of v_t.

The materials with large electron-hole asymmetry are known to enhance the thermoelectric coefficient. So more thermopower is expected when the middle region is made of a tilted Dirac material instead of graphene. But v_t does not break the electron-hole symmetric nature in $\mathcal{T}_\zeta(\epsilon)$ as shown in Fig. 4. Hence, it cannot aid in enhancing the thermopower of the system. It is to be noted that if the middle region is also monolayer graphene, then for a higher value of η, we do not get any thermopower in the low chemical potential regime, whereas if the middle region is borophene or quinoid graphene, we get finite values of thermopower for those low values of the chemical potential. The physics behind this is as follows: For graphene, in the case of $\epsilon < |\Delta_\zeta|$, there is no transmission because of imaginary momentum, and thus no channel to conduct. But for borophene or quinoid graphene, due to the indirect gap for the tilted velocity term, the momentum is real until $\epsilon > |\gamma_\zeta/2|$, and hence few channels are available to conduct, although $\epsilon < |\Delta_\zeta|$ [see Eq. (6) and Fig. 2]. Thus for a low chemical potential, the highly gapped graphene-borophene-graphene junction is a good candidate with respect to the highly gapped graphene-graphene-graphene junction as a thermoelectric device.

C. Valley thermal conductance

The valley-polarized thermal conductance k_v^{el} and charge thermal conductance k_c^{el} as a function of μ are shown in Figs. 7(a) and 7(b), respectively, for different values of η.

1. Dependence on chemical potential

As the valley-resolved thermal conductance k_ζ^{el} arises due to the energy flow carried by the charge carriers, $k_{v/c}^{\text{el}}$ as a function of μ shows almost similar features as $G_{v/c}$ except for the region where μ is close to zero. In the case of $k_{v/c}^{\text{el}}$ [see Figs. 7(a) and 7(b)] there is a bump near $\mu = 0$, while for $G_{v/c}$ there is no such thing. This bump in $k_{v/c}^{\text{el}}$ arises due to the $(k^{\text{el}})_V$ term as shown in the inset of Fig. 7(b), whereas valley $(k^{\text{el}})_T$ [in addition to valley $(k^{\text{el}})_V$] is also responsible for the bump in k_v^{el} [see the inset of Fig. 7(a)]. Moreover, the valley thermal conductance k_v^{el} has peaks at $\pm \mu_p(\eta)$ and then starts decreasing with μ (similar to G_v), as opposed to k_c^{el}.
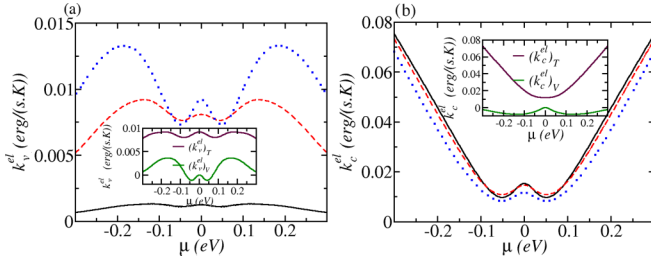
FIG. 7. Variation of (a) electrical valley thermal conductance k_v^{el} and (b) electrical thermal conductance k_c^{el} as a function of chemical potential μ for different values of η: $\eta = 0.1$ (black solid), $\eta = 0.8$ (red dashed), and $\eta = 1.5$ (blue dotted).

2. Dependence on gap parameter

As expected, k^{el} shows the same nature as the electrical charge conductance as a function of η, which is depicted in Fig. 7. The reason behind this nature is the same as for the charge conductance.

Not surprisingly, k^{el} as a function of v_t shows similar behavior as the electrical charge conductance, indicating that electrical thermal conductance is diminished by v_t. Here, we would like to mention that in our system, the Wiedmann-Franz law which states that $\sigma_c / \kappa_c = LT$, where $L = 2.44 \times 10^{-8}$ W Ω K^{-1} is the Lorentz number, σ_c is electrical charge conductivity, and κ_c is the electrical thermal conductivity, holds well for low temperature, though it deviates near $\mu = 0$. This law is valid in the case of valley-polarized conductivities as well under the same conditions.

D. Valley figure of merit

The variation of the valley and charge figures of merit $Z_v T$ and $Z_c T$ with μ are shown in Figs. 8(a) and 8(b), respectively, for different values of η.

1. Dependence on chemical potential

Both figures of merit show similar behavior as a function of μ and have maxima close to $\mu \sim \pm 0.06$ eV. The occurrence of maxima can be explained as follows: From the definition of ZT, we see that ZT varies as S^2. Since S_v and S_v attain extrema near $\mu \sim \pm 0.06$ eV (see Sec. III B 1), $Z_v T$ and $Z_c T$ are also peaked around those values for the given set of
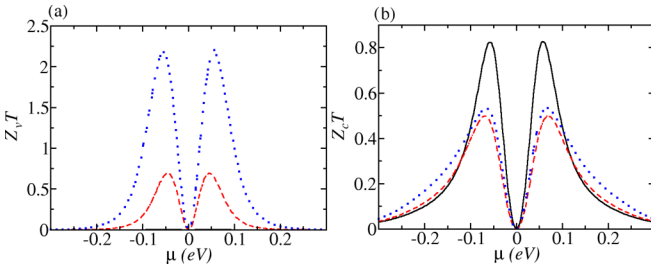

FIG. 8. Variation of (a) valley figure of merit $Z_v T$ and (b) charge figure of merit $Z_c T$ as a function of chemical potential μ for different values of η: $\eta = 0.1$ (black solid), $\eta = 0.8$ (red dashed), and $\eta = 1.5$ (blue dotted).

parameters. The positions of the peaks are almost insensitive to the gap parameter η.

2. Dependence on gap parameter

An increase in η enhances $Z_v T$, because $Z_v T$ mainly varies as S_v^2 which shows an increasing trend with η. For $\eta \to 0$, $Z_v T \to 0$ as the valley thermopower S_v vanishes. The charge figure of merit behaves nonmonotonically with η for $|\mu| < 0.1$ eV, while for $|\mu| > 0.1$ eV it increases with η, thereby depicting the trend of S_c^2. For $|\mu| < 0.1$ eV, the $Z_c T$ decreases with η (for $\eta < 1$), becomes minimum at $\eta = 0$, and starts to increase again for $\eta > 1$.

It is observed that both $Z_v T$ and $Z_c T$ get reduced with an increase in v_t. This is attributed to the fact that an increase in v_t reduces the thermopower (see Sec. III B) while the ratio of G and k^{el} does not vary appreciably with v_t. For the parameters used in the problem, the maximum values of $Z_v T$ and $Z_c T$ are 2.2 and 0.82, respectively. With the inclusion of the phonon's thermal conductance using the value in Ref. [66], $(Z_v T)_{max}$ and $(Z_c T)_{max}$ are reduced to ~ 1.84 and ~ 0.67, respectively. However, the value mentioned in Ref. [66] is for pristine borophene, whereas our system is a heterojunction with a band gap in the dispersion of the middle region. Thus the values are not accurate, but rather an estimation.

Here, we would like to mention that the structure of borophene is anisotropic along the x and y directions and it affects the transport properties in two directions differently. For the bulk borophene cases in Ref. [35], the electrical and thermal conductances in two directions differ quantitatively rather than qualitatively, while the results obtained for the thermopower and figure of merit are almost direction independent. Since the results in both directions are qualitatively the same, we have presented the results for the isotropic case.

IV. CONCLUSION

We propose a graphene/gapped tilted Dirac material/graphene junction which may exhibit a valley Seebeck effect when the middle region is irradiated with off-resonant circularly polarized light. The effect arises due to unequal gaps at the two valleys caused by a combination of the Semenoff mass M and photoinduced mass $\zeta \Delta$, where ζ is the valley index. Valley-polarized thermoelectric properties arise in the device owing to unequal transmission probabilities in the conducting channels of the nondegenerate valleys. We have studied the valley caloritronics of this junction device in a systematic framework and compared the results with the corresponding charge caloritronics. In particular, we have studied the dependence of the chemical potential μ and the role of a tunable gap parameter $\eta = M/\Delta$ in the electrical and thermal conductances, the Seebeck coefficient (thermopower), and the figure of merit of this junction. Since the renormalized radiation amplitude $\beta (= eA_0 a/\hbar) \sim 0.1 \ll 1$ under an off-resonant approximation (see Appendix A), the contributions from the nonzero order Floquet sidebands in the transport properties of the system have been neglected.

The valley-polarized electrical conductance G_v attains a maximum and then decreases asymptotically to zero while

the total charge conductance G_c increases monotonically with the chemical potential (μ). Furthermore, G_v increases with η for $\eta < 1$ and decreases with η for $\eta > 1$, while G_c shows a decreasing trend with η. The electrical thermal conductance κ^{el} as a function of η and μ shows almost similar behavior as the charge conductance, as it is proportional to the amount of heat energy carried by the charge carriers. Both valley (S_v) and charge Seebeck coefficients (S_c) attain maximum values at $\mu \sim \pm 0.04$ eV, which is roughly independent of η. But S_v increases with η, while S_c shows a nonmonotonic nature for $|\mu| < 0.08$ eV. For $|\mu| < 0.08$ eV, the S_c shows minimum values at $\eta = 1$ and starts to gain weight as we decrease (for $\eta < 1$) or increase η (for $\eta > 1$). For $|\mu| > 0.08$ eV, an increase in η leads to a small enhancement in S_c.

Since the ratio of G and κ does not show any significant change with η, the figure of merit as a function of η shows a variation similar to the square of thermopower and its maximum value is obtained at $\mu = \pm 0.06$ eV. We have also analyzed the effect of tilting in the thermoelectric properties. The tilt parameter v_t reduces the effective transmission through the junction, thereby diminishing all the charge- and valley-polarized quantities.

The exploitation of the valley thermoemf for thermoelectric power generation may serve as another development in the field of valley caloritronics. Since the photoinduced mass Δ and Semenoff mass M can be adjusted by varying the intensity of the light source and the strength of the inversion symmetry-breaking electric field, respectively, the tuning of the gap parameter η may be achievable in an experimental setup.

APPENDIX A: FLOQUET HAMILTONIAN OF A TILTED DIRAC MATERIAL SUBJECTED TO CIRCULARLY POLARIZED RADIATION

The Hamiltonian for quasiparticles with massive tilted anisotropic Dirac dispersion in the vicinity of two independent Dirac points in materials such as borophene or quinoid graphene is given by [27–29,37]

$$H_B(\mathbf{q}) = \zeta \hbar [v_x \sigma_x q_x + \zeta v_y \sigma_y q_y + v_t \sigma_0 q_y] + M\sigma_z, \quad \text{(A1)}$$

where σ_x, σ_y are the Pauli matrices, σ_0 is the 2×2 identity matrix, and $\zeta = \pm$ denotes the two independent Dirac points. $M\sigma_z$ is the mass term due to different on-site energies ($\pm M$) of the two sublattices. The energy dispersion and the corresponding wave functions associated with the Hamiltonian in Eq. (A1) are given by

$$E_{\lambda,\zeta}(\mathbf{q}) = \hbar \zeta v_t q \sin \theta + \lambda \sqrt{M^2 + [\hbar q \Lambda(\theta)]^2} \quad \text{(A2)}$$

and

$$\Psi_B^{\lambda,\zeta}(\mathbf{r}) = \frac{e^{i\mathbf{q}\cdot\mathbf{r}}}{\sqrt{2}} \begin{pmatrix} 1 \\ \frac{\zeta \hbar q \Lambda(\theta) e^{i\zeta\delta}}{M + \lambda\sqrt{M^2 + [\hbar q \Lambda(\theta)]^2}} \end{pmatrix}, \quad \text{(A3)}$$

where $\delta = \tan^{-1}[v_y q_y/(v_x q_x)]$, $\theta = \tan^{-1}(q_y/q_x)$, $\Lambda(\theta) = \sqrt{(v_x \cos \theta)^2 + (v_y \sin \theta)^2}$, and $\lambda = \pm$ denotes the conduction and valence bands, respectively. Note that the $v_t \neq 0$ term tilts the Dirac spectrum and is responsible for the electron-hole symmetry breaking, even for the $v_x = v_y$ case.

Consider the borophene sheet is illuminated normally by intense circularly polarized electromagnetic radiation. The vector potential corresponding to the circularly polarized radiation is given by $\mathbf{A}(t) = A_0(\hat{\mathbf{i}} \sin \omega t + \hat{\mathbf{j}} \cos \omega t)$, where $A_0 = E_0/\omega$, with E_0 being the amplitude of the electric field vector and ω is the frequency of the radiation. The vector potential is time periodic since $\mathbf{A}(t + T_\omega) = \mathbf{A}(t)$, with the time period $T_\omega = 2\pi/\omega$.

The time-periodic Hamiltonian in the presence of electromagnetic radiation is given by

$$H_B(\mathbf{q}, t) = \zeta \hbar [v_x \sigma_x Q_x(t) + \zeta v_y \sigma_y Q_y(t) + v_t \sigma_0 Q_y(t)] + M\sigma_z, \quad \text{(A4)}$$

where $Q_i = q_i + eA_i(t)/\hbar$ with $i = x, y$. It is known that a gap in the Dirac spectrum can be induced in graphene, on the surface states of a topological insulator, silicene, semi-Dirac systems, MoS_2, etc., by off-resonant radiation. The off-resonant condition is achieved when the photon energy ($\hbar\omega$) is much higher than the bandwidth (6τ with τ being the nearest-neighbor hopping energy) of the undriven borophene. In the off-resonant condition, the band structure is modified by the second-order virtual photon absorption-emission processes. The effective time-independent Floquet Hamiltonian in the off-resonant limit can be expressed as [67–69]

$$H_F(\mathbf{q}) \simeq H_B(\mathbf{q}) + \frac{[H_{-1}(\mathbf{q}), H_{+1}(\mathbf{q})]}{\hbar\omega}, \quad \text{(A5)}$$

where the terms in the commutator are the Fourier components of $H(\mathbf{q}, t)$,

$$H_{\pm 1}(\mathbf{q}) = \frac{1}{T_\omega} \int_0^{T_\omega} dt\, e^{\mp i\omega t} H(\mathbf{q}, t). \quad \text{(A6)}$$

Using Eq. (A6) we find the commutator $[H_{-1}, H_{+1}]$ as given below,

$$\frac{[H_{-1}(\mathbf{q}), H_{+1}(\mathbf{q})]}{\hbar\omega} = \frac{\zeta e^2 A_0^2 v_x v_y}{\hbar\omega} \sigma_z = \zeta \Delta \sigma_z, \quad \text{(A7)}$$

where $\Delta = (eA_0)^2 v_x v_y/(\hbar\omega)$ is the gap at the Dirac points, an experimentally tunable parameter. The gap parameter Δ does not depend on the tilt parameter v_t.

Here, we would like to mention that the scattering by the Floquet sidebands are neglected in our study due to the off-resonant condition of light. For off-resonant light, the nth-($n \neq 0$) order Floquet sidebands are separated from zeroth-order bands (static modes) by large quasienergies ($\sim n\hbar\omega$). As discussed in Ref. [54], the inelastic scatterings, i.e., photon absorptions and emissions between the sidebands, are suppressed by a factor of β^2, where $\beta = eA_0 a/\hbar$ is the renormalized radiation amplitude, with a being the lattice constant. Also, the transmission coefficients for sidebands of order $n \neq 0$ are small $\sim \mathcal{O}(\beta^{2n})$. In our system, the value of β for the chosen parameters to evaluate Δ is ~ 0.1. Thus, the modification in transmission probability due to the scattering by the Floquet sidebands is negligibly small.

APPENDIX B: TRANSMISSION PROBABILITY

In this Appendix, we provide the derivation of the transmission probability of the electron along with some plots of transmission probability (as a function of incident angle) which are required to justify the results presented in Figs. 3 and 4.

The wave functions in the three different regions, $\Psi_1(x, y)$, $\Psi_2(x, y)$, and $\Psi_3(x, y)$, will have the same y dependence: $\Psi_i(x, y) = \Psi_i(x)e^{ik_y y}$ with $i = 1, 2, 3$. The wave functions $\Psi_1(x)$, $\Psi_2(x)$, and $\Psi_3(x)$ for the three different regions for A and B sublattices can be written in the following forms: for $x < 0$,

$$\Psi_1^\zeta(x) = \begin{pmatrix} e^{ik_x x} \\ \zeta e^{ik_x x + i\zeta \phi} \end{pmatrix} + r_\zeta \begin{pmatrix} e^{-ik_x x} \\ -\zeta e^{-ik_x x - i\zeta \phi} \end{pmatrix}, \quad (B1)$$

for $0 < x < L$,

$$\Psi_2^\zeta(x) = a_\zeta \begin{pmatrix} e^{iq_x x} \\ \zeta p_\zeta e^{iq_x x + i\zeta \delta} \end{pmatrix} + b_\zeta \begin{pmatrix} e^{-iq_x x} \\ -\zeta p_\zeta e^{-iq_x x - i\zeta \delta} \end{pmatrix}, \quad (B2)$$

and for $x > L$,

$$\Psi_3^\zeta(x) = t_\zeta \begin{pmatrix} e^{ik_x x} \\ \zeta e^{ik_x x + i\zeta \phi} \end{pmatrix}. \quad (B3)$$

Here, the expression for p_ζ is given by

$$p_\zeta = \frac{\hbar q \Lambda(\theta)}{\Delta_\zeta + \sqrt{\Delta_\zeta^2 + [\hbar q \Lambda(\theta)]^2}}. \quad (B4)$$

The valley-dependent reflection amplitude r_ζ and the transmission amplitude t_ζ are obtained by matching the wave functions at the interfaces $x = 0$ and $x = L$,

$$\Psi_1^\zeta(x = 0) = \Psi_2^\zeta(x = 0), \quad \Psi_2^\zeta(x = L) = \Psi_3^\zeta(x = L). \quad (B5)$$

From the above conditions, the valley-dependent transmission probability $\mathcal{T}_\zeta(\epsilon, \phi) = |t_\zeta(\epsilon, \phi)|^2$ is obtained as

$$\mathcal{T}_\zeta(\epsilon, \phi) = \frac{4p_\zeta^2 \cos^2 \phi (1 + \cos 2\delta)}{\left(2\sqrt{2} p_\zeta \cos \phi \cos \delta\right)^2 + \left[1 + p_\zeta^2 - 2p_\zeta \cos(\phi - \delta)\right]\left[1 + p_\zeta^2 + 2p_\zeta \cos(\phi + \delta)\right][1 - \cos(2qL \cos \theta)]}. \quad (B6)$$

Here, it should be noted that there is no mechanism present in the junction that mixes states of opposite valleys. The system can be reduced to a gapless single graphene sheet by setting $\Delta_\zeta = 0$, $v_t = 0$, and $v_x = v_y = v_F$. In this limiting case, it can be easily checked that $\mathcal{T}_\zeta(\epsilon, \phi) = 1$.

To understand the behavior of $\mathcal{T}_\zeta(\epsilon)$ (Figs. 3 and 4), plots for $\mathcal{T}_\zeta(\epsilon, \phi)$ for different conditions as a function of the incident angle ϕ for a fixed energy $\epsilon = 0.5$ eV and $L = 50$ nm are shown in Figs. 9–11.

Figures 9 and 10 show plots of $\mathcal{T}_\zeta(\epsilon, \phi)$ as a function of ϕ for (i) $v_t = 0$, $v_x \neq v_y$ and (ii) $v_t = 0$, $v_x = v_y = v_F$ for two values of η with Δ fixed at 0.05 eV. On the other hand, Fig. 11 shows a plot of $\mathcal{T}_\zeta(\epsilon, \phi)$ as a function of ϕ for $v_t \neq 0$, $v_x \neq v_y$. All the figures show that the transmission probability is close to unity around the normal incidence ($\phi \to 0$) for both valleys. This is a manifestation of perfect tunneling when the incident wave vector is normal to the interface. Figure 9 shows that the transmission is allowed over the full range of the incident angle ($-\pi/2 \leqslant \phi \leqslant \pi/2$), whereas for Fig. 10 the transmission is restricted below the lower critical angle and above the upper critical angle. Further, in Fig. 11, the trans-
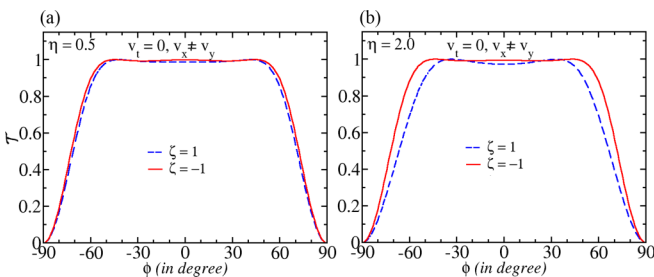
mission probability for $\zeta = +/-$ ceases to zero above/below some critical incident angles. This is because of $\sin \theta > 1$, as shown in the inset of Fig. 11, for which above or below the critical angles the wave vector in the middle region becomes complex, which leads to an evanescent wave. Figures 10 and 11 reveal that the allowed range of incident angles for $\zeta = -1$ is bigger than that for $\zeta = 1$, as for the latter one, the band gap is wider. It is clear that the value of the critical angles depends on all the three velocities v_x, v_y, and v_t. Similar critical angles exist in other semiconductor junction devices [70,71].

APPENDIX C: THEORY OF THERMOELECTRICITY

In this Appendix, we present the derivation of thermopower and the electron's thermal conductance in terms of the transmission probability.

Assuming that the graphene leads are independent electron reservoirs, the chemical potential and the temperature of the left/right graphene leads are $\mu_{L/R}$ and $T_{L/R}$, respectively. The population of electrons at the left/right leads is described by the Fermi-Dirac distribution function $f_{L/R} = f(\mu_{L/R}, T_{L/R}) = [1 + e^{(\epsilon - \mu_{L/R})/(k_B T_{L/R})}]^{-1}$. Employing the Landauer-Buttiker

FIG. 9. Transmission probability $\mathcal{T}_\zeta(\epsilon, \phi)$ as a function of incident angle ϕ for (a) $\eta = 0.5$, (b) $\eta = 2$ when $v_t = 0$, $v_x \neq v_y$.
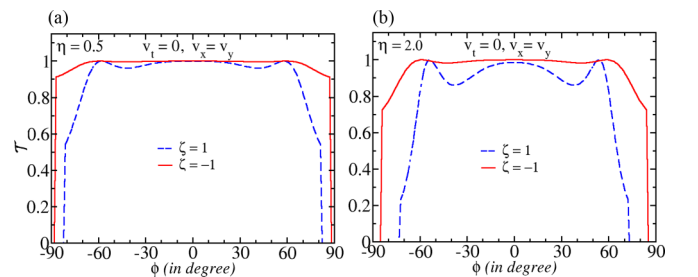

FIG. 10. Transmission probability $\mathcal{T}_\zeta(\epsilon, \phi)$ as a function of incident angle ϕ for (a) $\eta = 0.5$, (b) $\eta = 2$ when $v_t = 0$, $v_x = v_y = v_F$.
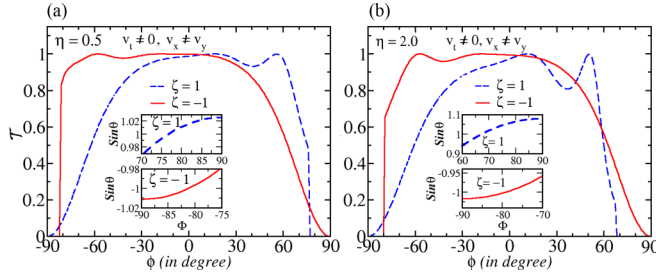
FIG. 11. Transmission probability $\mathcal{T}_\zeta(\epsilon, \phi)$ as a function of incident angle ϕ for (a) $\eta = 0.5$, (b) $\eta = 2$ when $v_t \neq 0$, $v_x \neq v_y$.

formalism in a quasiballistic regime, the valley-dependent charge current is given by

$$I_\zeta = \frac{2e}{h} \int_{-\pi/2}^{\pi/2} d\phi \cos\phi \int_{-\infty}^{\infty} N(\epsilon)\mathcal{T}_\zeta(\epsilon, \phi)(f_L - f_R)d\epsilon, \quad \text{(C1)}$$

where $N(\epsilon) = W|\epsilon|/(\pi\hbar v_F)$ is the energy-dependent number of transverse modes in the graphene sheet of width W [72]. Here, it has been used that $\mathcal{T}_{L,\zeta}(\epsilon, \phi) = \mathcal{T}_{R,\zeta}(\epsilon, \phi) = \mathcal{T}_\zeta(\epsilon, \phi)$ with $T_{L,\zeta}(\epsilon, \phi)$ [$T_{R,\zeta}(\epsilon, \phi)$] is the transmission probability of an electron with energy ϵ and incidence angle ϕ from the left (right) graphene leads.

In the absence of any external bias voltage (V_B), the chemical potentials of the two leads are taken to be the same as $\mu_L = \mu_R = \mu$. Due to the applied temperature difference (dT) between the two leads, there will be a small voltage difference (dV) between the leads. The currents induced by dT and dV are given by $(dI_\zeta)_T = I_\zeta(\mu, T; \mu, T + dT)$ and $(dI_\zeta)_V = I_\zeta(\mu, T; \mu + edV, T)$, where the currents $I_\zeta(\mu, T; \mu, T + dT)$ and $I_\zeta(\mu, T; \mu + edV, T)$ can be calculated from Eq. (C1). Since in an open circuit condition the current cannot flow, one can write

$$dI_\zeta = (dI_\zeta)_T + (dI_\zeta)_V = 0. \quad \text{(C2)}$$

Expanding the Fermi-Dirac distribution functions in Eqs. (C1) and (C2) in the linear response regime, i.e., up to the first-order terms in dV and dT, one can get the valley-resolved

Seebeck coefficient S_ζ as

$$S_\zeta = -\frac{dV}{dT}\bigg|_{dI_\zeta=0} = -\frac{L_\zeta^{(1)}}{eTL_\zeta^{(0)}}, \quad \text{(C3)}$$

where the kinetic coefficients $L_\zeta^{(\alpha)}$ for the quasiballistic transport regime are given by

$$L_\zeta^{(\alpha)} = \int_{-\pi/2}^{\pi/2} d\phi \cos\phi \int_{-\infty}^{\infty} \mathcal{T}_\zeta(\epsilon, \phi)N(\epsilon)(\epsilon-\mu)^\alpha \left(-\frac{\partial f}{\partial\epsilon}\right)d\epsilon, \quad \text{(C4)}$$

with $\alpha = 0, 1, 2$.

The flow of electrons can also transport thermal energy through the junction, which is responsible for the thermal current. The electron's thermal current is the energy current carried by electrons traveling between leads driven by $dT = T_R - T_L$ and $dV = (\mu_R - \mu_L)/e$. Analogous to the charge current, the electron's valley-resolved thermal current can be written as

$$J_\zeta^{\text{el}} = \frac{2}{h} \int_{-\pi/2}^{\pi/2} d\phi \cos\phi \int_{-\infty}^{\infty} N(\epsilon)\mathcal{T}_\zeta(\epsilon, \phi)(\epsilon - \mu)(f_L - f_R)d\epsilon. \quad \text{(C5)}$$

Analogous to the charge current driven by dT and dV, the electron's valley-resolved thermal current can be written as

$$dJ_\zeta^{\text{el}} = (dJ_\zeta^{\text{el}})_T + (dJ_\zeta^{\text{el}})_V, \quad \text{(C6)}$$

where $(dJ_\zeta^{\text{el}})_T = J_\zeta^{\text{el}}(\mu, T; \mu, T + dT)$ and $(dJ_\zeta^{\text{el}})_V = J_\zeta^{\text{el}}(\mu, T; \mu + edV, T)$. Note that dV is generated by the Seebeck effect due to the temperature difference dT. Both $J_\zeta^{\text{el}}(\mu, T; \mu, T + dT)$ and $J_\zeta^{\text{el}}(\mu, T; \mu + edV, T)$ can be calculated using Eq. (C5). Similarly, the electron's thermal conductance $k_\zeta^{\text{el}} = dJ_\zeta^{\text{el}}/dT$ has two components,

$$k_\zeta^{\text{el}} = (k_\zeta^{\text{el}})_T + (k_\zeta^{\text{el}})_V, \quad \text{(C7)}$$

where $(k_\zeta^{\text{el}})_T = (dJ_\zeta^{el})_T/dT$ and $(k_\zeta^{\text{el}})_V = (dJ_\zeta^{\text{el}})_V/dT$ are the portions of the electron's thermal conductance driven by dT and dV, respectively. The electron's valley-resolved thermal conductance can be expressed in terms of the kinetic coefficients $L_\zeta^{(\alpha)}$ [as given in (C4)] [59,60] as

$$k_\zeta^{\text{el}} = \frac{2}{h}\frac{L_\zeta^{(2)}}{T} + \frac{2e}{h}L_\zeta^{(1)}S_\zeta. \quad \text{(C8)}$$

[1] L. D. Hicks and M. S. Dresselhaus, Phys. Rev. B **47**, 12727 (1993).

[2] L. D. Hicks and M. S. Dresselhaus, Phys. Rev. B **47**, 16631 (1993).

[3] R. Venkatasubramanian, E. Siivola, T. Colpitts, and B. O'Quinn, Nature (London) **413**, 597 (2001).

[4] R. Arita, K. Kuroki, K. Held, A. V. Lukoyanov, S. Skornyakov, and V. I. Anisimov, Phys. Rev. B **78**, 115121 (2008).

[5] N. Hamada, T. Imai, and H. Funashima, J. Phys.: Condens. Matter **19**, 365221 (2007).

[6] J. M. O. Zide, D. Vashaee, Z. X. Bian, G. Zeng, J. E. Bowers, A. Shakouri, and A. C. Gossard, Phys. Rev. B **74**, 205335 (2006).

[7] P. Wei, W. Bao, Y. Pu, C. N. Lau, and J. Shi, Phys. Rev. Lett. **102**, 166808 (2009).

[8] Y. M. Zuev, W. Chang, and P. Kim, Phys. Rev. Lett. **102**, 096807 (2009).

[9] T. Kato, S. Usui, and T. Yamamoto, Jpn. J. Appl. Phys. **52**, 06GD05 (2013).

[10] M. Buscema, M. Barkelid, V. Zwiller, H. S. J. van der Zant, G. A. Steele, and A. Castellanos-Gomez, Nano Lett. **13**, 358 (2013).

[11] S. Konabe and T. Yamamoto, Phys. Rev. B **90**, 075430 (2014).

[12] L. D. Hicks, T. C. Harman, X. Sun, and M. S. Dresselhaus, Phys. Rev. B **53**, R10493(R) (1996).

[13] M. S. Dresselhaus, G. Chen, M. Y. Tang, R. Yang, H. Lee, D. Wang, Z. Ren, J.-P. Fleurial, and P. Gogna, Adv. Mater. **19**, 1043 (2007).

[14] D. Bilc, S. D. Mahanti, K. F. Hsu, E. Quarez, R. Pcionek, and M. G. Kanatzidis, Phys. Rev. Lett. **93**, 146403 (2004).

[15] J. P. Heremans, V. Jovovic, E. S. Toberer, A. Saramat, K. Kurosaki, A. Charoenphakdee, S. Yamanaka, and G. J. Snyder, Science **321**, 554 (2008).

[16] W.-S. Liu, L.-D. Zhao, B.-P. Zhang, H.-L. Zhang, and J.-F. Li, Appl. Phys. Lett. **93**, 042109 (2008).

[17] M. Markov, X. Hu, H.-C. Liu, N. Liu, S. J. Poon, K. Esfarjani, and M. Zebarjadi, Sci. Rep. **8**, 9876 (2018).

[18] A. K. Geim and K. S. Novoselov, Nat. Mater. **6**, 183191 (2007).

[19] D. Pesin and A. H. MacDonald, Nat. Mater. **11**, 409 (2012).

[20] B. Feng, H. Li, C. Liu, T. Shao, P. Cheng, Y. Yao, S. Meng, L. Chen, and K. Wu, ACS Nano **7**, 9049 (2013).

[21] R. Quhe, Y. Yuan, J. Zheng, Y. Wang, Z. Ni, J. Shi, D. Yu, J. Yang, and J. Lu, Sci. Rep. **4**, 5476 (2014).

[22] K. F. Mak, C. Lee, J. Hone, J. Shan, and T. F. Heinz, Phys. Rev. Lett. **105**, 136805 (2010).

[23] A. J. Mannix, X. F. Zhou, B. Kiraly, J. D. Wood, D. Alducin, B. D. Myers, X. Liu, B. L. Fisher, U. Santiago, J. R. Guest, M. J. Yacaman, A. Ponce, A. R. Oganov, M. C. Hersam, and N. P. Guisinger, Science **350**, 1513 (2015).

[24] L. Xu, A. Du, and L. Kou, Phys. Chem. Chem. Phys. **18**, 27284 (2016).

[25] X. F. Zhou, X. Dong, A. R. Oganov, Q. Zhu, Y. Tian, and H. T. Wang, Phys. Rev. Lett **112**, 085502 (2014).

[26] A. Lopez-Bezanilla and P. B. Littlewood, Phys. Rev. B **93**, 241405(R) (2016).

[27] A. D. Zabolotskiy and Y. E. Lozovik, Phys. Rev. B **94**, 165403 (2016).

[28] M. Nakhaee, S. A. Ketabi, and F. M. Peeters, Phys. Rev. B **97**, 125424 (2018).

[29] M. O. Goerbig, Rev. Mod. Phys. **83**, 1193 (2011).

[30] M. O. Goerbig, J.-N. Fuchs, G. Montambaux, and F. Piéchon, Phys. Rev. B **78**, 045415 (2008).

[31] S. Verma, A. Mawrie, and T. K. Ghosh, Phys. Rev. B **96**, 155418 (2017).

[32] SK Firoz Islam and A. M. Jayannavar, Phys. Rev. B **96**, 235405 (2017).

[33] Z. Jalali-Mola and S. A. Jafari, Phys. Rev. B **98**, 195415 (2018).

[34] A. E. Champo and G. G. Naumis, Phys. Rev. B **99**, 035415 (2019).

[35] M. Zare, Phys. Rev. B **99**, 235413 (2019).

[36] B. Feng, O. Sugino, R.-Y. Liu, J. Zhang, R. Yukawa, M. Kawamura, T. Iimori, H. Kim, Y. Hasegawa, H. Li *et al.*, Phys. Rev. Lett. **118**, 096401 (2017).

[37] M. Ezawa, Phys. Rev. B **96**, 035425 (2017).

[38] X. Liu and M. C. Hersam, Sci. Adv. **5**, 6444 (2019).

[39] L. Zhang, K. Gong, J. Chen, L. Liu, Y. Zhu, D. Xiao, and H. Guo, Phys. Rev. B **90**, 195428 (2014).

[40] J. Wang, K. S. Chan, and Z. Lin, Appl. Phys. Lett. **104**, 013105 (2014).

[41] Z. P. Niu and S. Dong, Appl. Phys. Lett. **104**, 202401 (2014).

[42] X. Chen, L. Zhang, and H. Guo, Phys. Rev. B **92**, 155427 (2015).

[43] K. Uchida, S. Takahasi, K. Harii, J. Ieda, W. Koshibae, K. Ando, S. Maekawa, and S. Saitoh, Nature (London) **455**, 778 (2008).

[44] C. M. Jaowrski, J. Yang Smack, D. D. Awschalom, J. P. Heremans, and R. C. Myers, Nat. Mater. **9**, 898 (2010).

[45] G. E. W. Bauer, A. H. Macdonald, and S. Maekawa, Solid State Commun. **150**, 459 (2010).

[46] G. E. W. Bauer, E. Saitoh, and B. J. Wees, Nat. Mater. **11**, 391 (2012).

[47] M. Hatami, G. E. W. Bauer, Q. F. Zhang, and P. J. Kelly, Phys. Rev. B **79**, 174426 (2009).

[48] X. B. Chen, Y. Z. Liu, B. L. Gu, W. H. Duan, and F. Liu, Phys. Rev. B **90**, 121403 (2014).

[49] W. Yao, D. Xiao, and Q. Niu, Phys. Rev. B **77**, 235406 (2008).

[50] T. Cao, G. Wang, W. Han, H. Ye, C. Jhu, J. Shi, Q. Niu, P. Tan, E. Wang, B. Liu, and J. Feng, Nat. Commun. **3**, 887 (2012).

[51] Y. J. Zhang, T. Oka, R. Suzuki, J. T. Ye, and Y. Iwasa, Science **344**, 725 (2014).

[52] K. F. Mak, K. L. McGill, J. Park, and P. L. McEuen, Science **344**, 1489 (2014).

[53] P. Sengupta, Y. Tan, E. Bellotti, and J. Shi, J. Phys.: Condens. Matter **30**, 435701 (2018).

[54] T. Kitagawa, T. Oka, A. Brataas, and L. Fu, and E. Demler, Phys. Rev. B **84**, 235108 (2011).

[55] F. D. M. Haldane, Phys. Rev. Lett. **61**, 2015 (1988).

[56] J. Jung, A. M. DaSilva, A. H. MacDonald, and S. Adam, Nat. Commun. **6**, 6308 (2015).

[57] X. Cao, J. Shi, M. Zhang, X. Jiang, H. Zhong, P. Huang, Y. Ding, and M. Wu, J. Phys. Chem. C **120**, 11299 (2016).

[58] R. Takahashi and S. Murakami, Phys. Rev. B **81**, 161302(R) (2010).

[59] A. Mawrie and B. Muralidharan, Phys. Rev. B **100**, 081403(R) (2019).

[60] Y. S. Liu, B. C. Hsu, and Y. C. Chen, J. Phys. Chem. **115**, 6111 (2011).

[61] R. Swirkowicz, M. Wierzbicki, and J. Barnas, Phys. Rev. B **80**, 195409 (2009).

[62] M. Wierzbicki, R. Swirkowicz, and J. Barnas, Phys. Rev. B **88**, 235434 (2013).

[63] B. Z. Rameshti and A. G. Moghaddam, Phys. Rev. B **91**, 155407 (2015).

[64] T. Tohei, A. Kuwabara, F. Oba, and I. Tanaka, Phys. Rev. B **73**, 064304 (2006).

[65] H. Zhou, Y. Cai, G. Zhang, and Y.-W. Zhang, npj 2D Mater. Appl. **1**, 14 (2017).

[66] H. Xiao, W. Cao, T. Ouyang, S. Guo, C. He, and J. Zhong, Sci. Rep. **7**, 45986 (2017).

[67] W. Magnus, Commun. Pure Appl. Math. **7**, 649 (1954).

[68] S. Blanes, F. Casas, J. A. Oteo, and J. Ros, Phys. Rep. **470**, 151 (2009).

[69] A. Lopez, A. Scholz, B. Santos, and J. Schliemann, Phys. Rev. B **91**, 125105 (2015).

[70] M. Khodas, A. Shekhter, and A. M. Finkelstein, Phys. Rev. Lett. **92**, 086602 (2004).

[71] M. I. Alomar and D. Sanchez, Phys. Rev. B **89**, 115422 (2014).

[72] C. W. J. Beenakker, Phys. Rev. Lett. **97**, 067007 (2006).